



# Influence of B-site compositional homogeneity on properties of $(K_{0.44}Na_{0.52}Li_{0.04})(Nb_{0.86}Ta_{0.10}Sb_{0.04})O_3$ -based piezoelectric ceramics

L. Ramajo <sup>a,\*</sup>, M. Castro <sup>a</sup>, A. del Campo <sup>b</sup>, J.F. Fernandez <sup>b</sup>, F. Rubio-Marcos <sup>b</sup>

<sup>a</sup> Instituto de Investigaciones en Ciencia y Tecnología de Materiales (INTEMA), Av. Juan B Justo 4302, B7608FDQ Mar del Plata, Argentina

<sup>b</sup> Electroceramic Department, Instituto de Cerámica y Vidrio, CSIC, Kelsen 5, 28049 Madrid, Spain

Received 14 November 2013; received in revised form 20 January 2014; accepted 2 February 2014

Available online 5 March 2014

## Abstract

The effect of B-site compositional homogeneity on microstructure, piezoelectric properties and dielectric behaviour of lead-free piezoelectric ceramics,  $(K_{0.44}Na_{0.52}Li_{0.04})(Nb_{0.86}Ta_{0.10}Sb_{0.04})O_3$ , is investigated. The B-site compositional homogeneity is evaluated by using an intermediate precursor obtained by solid state reaction between adequate amounts of  $Nb_2O_5$ ,  $Ta_2O_5$  and  $Sb_2O_5$ , calcined at 1350 °C and attrition milled. The B-site precursor powder is mixed with alkaline carbonates to synthesize perovskite powders and, finally, sinter piezoceramics. X-ray diffraction and Raman spectroscopy reveal the formation of a perovskite phase, although tetragonal tungsten-bronze structure is detected as minor secondary phase. Ceramics processed by using B-site precursor show different crystalline structure as a function of sintering conditions or K/Na ratio. The B-site precursor route produces thus lower piezoelectric properties, but the control of alkali volatilization by using sintering powder bed resulted in a relevant decrease of dielectric losses that favours the  $d_{33}$  enhancement.

© 2014 Elsevier Ltd. All rights reserved.

**Keywords:** Lead-free piezoelectrics; KNL–NTS; Piezoelectric ceramics

## 1. Introduction

Potassium niobate ceramics,  $KNbO_3$ , present acceptable dielectric and piezoelectric properties. Particularly, niobates as  $(K_xNa_{1-x})NbO_3$ , KNN-based ceramics, show good piezoelectric and electric properties, high Curie temperature and are environmentally friendly.<sup>1,2</sup> When  $x = 0.5$  the piezoelectric coefficients reach the highest point ( $d_{33} \sim 80\text{ pC/N}$ ).<sup>3,4</sup> However, the application of these ceramics is limited by their poor sinterability due to the volatility of alkaline elements, and the high sensitivity of properties to stoichiometry.

Saito et al. reported exceptionally high piezoelectric properties in the system  $(K,Na)NbO_3$ – $LiTaO_3$ – $LiSbO_3$ .<sup>1</sup> This study was based on chemical modifications, in the vicinity of the morphotropic phase boundary (MPB) of KNN, by complex simultaneous substitutions in the A (Li) and B (Ta and Sb) sites

of the perovskite lattice. KNN-based ceramics having 4 mol% of lithium, 10 mol% of tantalum and 4 mol% of antimony prepared by solid state reaction produce nanopowders with good sinterability that reach interesting piezoelectric properties.<sup>5</sup>

The optimization of milling conditions, new sintering techniques and engineering of oriented structures have been followed to improve the microstructure.<sup>6,7</sup> However, some problems still exist in this family, among them: the strong tendency for anomalous grain growth; the lack of control on alkali volatilization; the limited range of temperatures for sintering dense ceramics; or the relatively poor reproducibility of the piezoelectric properties.<sup>8</sup>

It is known that the compositional inhomogeneity, particularly the inhomogeneous distribution of Nb, Ta and Sb on the B-site of the perovskite lattice, is rather difficult to be avoided due to the phase segregation of end members over a wide temperature interval.<sup>9</sup> In addition, apparent compositional segregation in KNN has been evidenced in ceramics annealed for a long time.<sup>10,11</sup>

In this work the effect of a B-site precursor on the final properties of  $(K_{0.44}Na_{0.52}Li_{0.04})(Nb_{0.86}Ta_{0.10}Sb_{0.04})O_3$  ceramics is investigated. Thus, the influence of the B-site compositional

\* Corresponding author. Tel.: +54 223 4816600; fax: +54 223 4814600.

E-mail addresses: [lramajo@fimdp.edu.ar](mailto:lramajo@fimdp.edu.ar), [lramajo@hotmail.com](mailto:lramajo@hotmail.com)  
(L. Ramajo).

inhomogeneity on the dielectric, ferroelectric, and piezoelectric properties is also evaluated and discussed.

## 2. Experimental

### 2.1. Preparation process

Two processing routes of  $(\text{K}_{0.44}\text{Na}_{0.52}\text{Li}_{0.04})(\text{Nb}_{0.86}\text{Ta}_{0.10}\text{Sb}_{0.04})\text{O}_3$  ceramics (hereafter abbreviated as KNL–NTS) were synthesized using the conventional solid-state reaction method.  $\text{Na}_2\text{CO}_3$ ,  $\text{Li}_2\text{CO}_3$  (Panreac, 99.5%),  $\text{K}_2\text{CO}_3$  (Merck, 99%),  $\text{Nb}_2\text{O}_5$ ,  $\text{Ta}_2\text{O}_5$ , and  $\text{Sb}_2\text{O}_5$  (Sigma–Aldrich, 99.9%, 99% and 99.995%, respectively), were used as starting raw materials. They were individually milled, in order to obtain an appropriate particle size distribution.<sup>12</sup> Because of their hygroscopic nature, raw materials were dried at 200 °C for 1 h before all experiments.

For **route I**, milled raw materials powders with KNL–NTS composition were mixed and attrition milled using Zirconia balls in ethanol for 3 h and then dried. For **route II**, the same conventional solid reaction method was used, although the oxides of B-site elements,  $\text{Nb}_2\text{O}_5$  and,  $\text{Sb}_2\text{O}_5$  and  $\text{Ta}_2\text{O}_5$ , were previously mixed and thermally treated at 1350 °C for 3 h to obtain a solid solution and thereafter attrition milled. The resulting B-site precursor was mixed with the adequate amount of alkali carbonates ball milled in ethanol for 3 h and then dried.

### 2.2. Thermal characterization

Powders of both routes were calcined at 700 °C for 2 h. The calcined powders were attrition milled again and pressed at 200 MPa into disks of 10 mm in diameter and 0.7 mm in thickness. Pellets of both routes were sintered at 1125 °C for 2 h. In addition, pellets of route II were sintered using a bed of the same calcined powder in order to produce a controlled atmosphere.

Simultaneous thermogravimetric and differential thermal analysis were carried out on powders corresponding to both routes by using a Netzsch STA 409 Analyzer. About 50 mg of powder was placed in a Pt/Rh crucible and heated up to 1200 °C at 3 °C/min. Measurements were performed in a flowing air atmosphere.

### 2.3. Structural characterization

Crystalline phases were characterized by X-ray diffraction (XRD) (D8 Advance, Bruker, Germany), using  $\text{CuK}_\alpha$  radiation. Raman spectra were measured in air atmosphere and at room temperature using a Confocal Raman Microscope, CRM, coupled to an AFM (Witec alpha-300R). Raman spectra were obtained using a 532 nm excitation laser and a 100× objective lens ( $\text{NA} = 0.9$ ). The incident laser power was 0.5 mW. The optical diffraction resolution of the Confocal Microscope was limited to about ~200 nm laterally and ~500 nm vertically. Raman spectral resolution of the system was down to 0.02  $\text{cm}^{-1}$ . Samples were deposited on a microscopy glass slide. The sample was mounted on a piezo-driven scan platform having a positional

accuracy of 4 nm lateral and 0.5 nm vertical. Collected spectra were analyzed by using Witec Control Plus Software.

### 2.4. Microstructural characterization

Microstructures were evaluated on polished and thermally etched samples (1000 °C for 5 min) using a Field Emission Scanning Electron Microscope, FE-SEM (Hitachi S-4700), equipped with energy dispersive spectroscopy, EDS. The average grain size was determined from FE-SEM micrographs by an image processing and analysis programme (Leica Qwin, Leica Microsystems Ltd., Cambridge, England) considering more than 100 grains in each measurement.

### 2.5. Electrical characterization

For the electrical measurements, a fired silver paste was used for the electric contacts. Samples were poled in a silicone oil bath at 25 °C by applying a DC field of 4.0 kV/mm<sup>-1</sup> for 30 min.<sup>13</sup> The piezoelectric constant  $d_{33}$  was measured using a piezo-d<sub>33</sub> meter (YE2730A d<sub>33</sub> METER, APC International, Ltd., USA). Dielectric properties were determined at different temperatures and frequencies using an Impedance Analyzer HP4294A in the frequency range of 100 Hz–1 MHz. Finally, the ferroelectric nature of these ceramics was determined using a hysteresis meter (RT 6000 HVS, RADIANT Technologies).

## 3. Results and discussion

### 3.1. Synthesis precursors: structural and thermal characterization

The X-ray diffraction pattern of the oxides of B-site precursor thermally treated at 1350 °C is shown in Fig. 1. The XRD pattern shows the diffraction peaks corresponding to solid monoclinic  $\text{Nb}_2\text{O}_5$  (PDF# 37-1468) where  $\text{Ta}^{5+}$  and  $\text{Sb}^{5+}$  may be included in the solid solution. On the other hand, the remaining secondary phase could be assigned to other crystalline structures of  $\text{Ta}_2\text{O}_5$  (PDF#33-1391) and unreacted  $\text{Sb}_2\text{O}_3$  (PDF#72-1334).

TG/DTA curves corresponding to KNL–NTS raw mixtures obtained by routes I and II are shown in Fig. 2. In the 25–1200 °C temperature range, both powder mixtures show a quite similar weight loss of ~12% corresponding to the same alkali carbonate content. However variations in the temperature and shape of the DTA peak are observed between both routes. In order to determine the temperature at which each phenomenon associated with weight loss occurs, the derivative of the weight loss curve is used and shown in the figure. Then, it is possible to observe four main weight losses associated with endothermic reactions taking place at 80 °C, 180 °C, 480 °C and 565 °C in the ceramics obtained by route I, which followed a conventional procedure. While for ceramics obtained by route II similar weight losses can be observed localized at 85 °C, 163 °C, 430 °C and 600 °C. The endothermic peaks at about ~80 °C are associated with the removal of absorbed environmental moisture, ~1 wt%. The endothermic peaks at ~180 °C for route I and ~163 °C for route II are related to simultaneous losses of  $\text{H}_2\text{O}$  and  $\text{CO}_2$ .<sup>14</sup> The

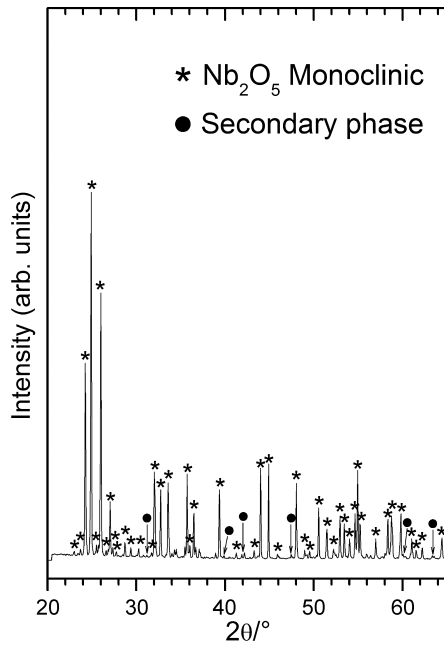


Fig. 1. XRD pattern corresponding to the B-site precursor thermally treated at 1350 °C. \*Monoclinic  $\text{Nb}_2\text{O}_5$  (PDF# 37-1468), and ● secondary phase. The secondary phase marked as (●) in figure, is composed of a mixture of  $\text{Ta}_2\text{O}_5$  and  $\text{Sb}_2\text{O}_5$ .

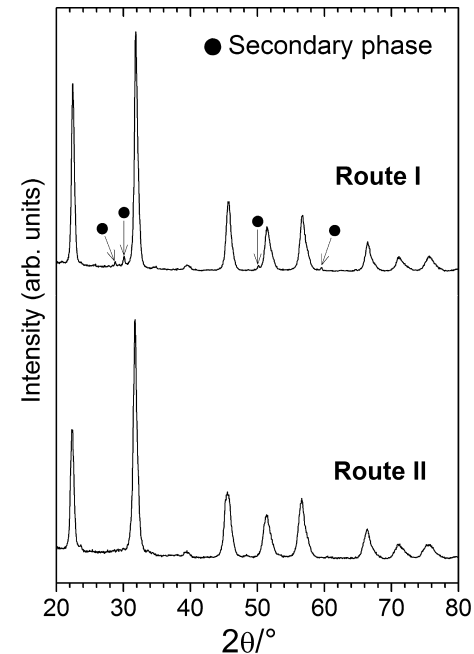


Fig. 3. Effect of the processing route on the structure of the KNL–NTS synthesized powders: XRD patterns of KNL–NTS powders obtained by conventional oxide mixture route (Route I) and by using B-site precursor (Route II).

$\text{AHCO}_3$  decomposition (where A is  $\text{K}^+$ ,  $\text{Na}^+$ ,  $\text{Li}^+$ ) to give  $\text{A}_2\text{CO}_3$  takes place in the temperature range of 100 to 180 °C,<sup>15</sup> with an associated weight loss of ~2%. The endothermic peak around 480 °C is related to the polymorphic phase transition of  $\text{A}_2\text{CO}_3$  (where A is  $\text{K}^+$ ,  $\text{Na}^+$ ,  $\text{Li}^+$ ).<sup>16</sup> Therefore, the KNL–NTS mixture losses  $\text{CO}_2$  in different temperatures stages between 180 °C and 600 °C. Finally, it can be observed that route II shows low decomposition temperatures between 150 and 500 °C, although the last decomposition appears at higher temperature with higher mass loss, suggesting that the B-sites precursor solution modifies the carbonate decomposition. These facts are indicative that the thermal treatment should be performed at temperatures over 650 °C. Based on these results; the heat treatment was selected

at 700 °C for 2 h, in order to guarantee the complete decomposition of the carbonates of the A-elements and pre-formation of the perovskite phase used in both methods.

Fig. 3 presents the X-ray diffraction patterns of KNL–NTS powders obtained from route I and route II and calcined at 700 °C for 2 h. These patterns reveal a main perovskite phase and a minor secondary phase, which is assigned to  $\text{K}_6\text{LiNb}_6\text{O}_{17}$  (PDF# 36-0533) or  $\text{K}_6\text{Nb}_{10.88}\text{O}_{30}$  (PDF# 87-1856), both with tetragonal tungsten-bronze phase structure (TTB).<sup>17</sup> This phase is more relevant in powders of route I, indicating that inhomogeneity in B-site could affect the formation of secondary phases. On the other hand, pre-forming solid solutions, route II improves the perovskite phase formation at lower temperatures.

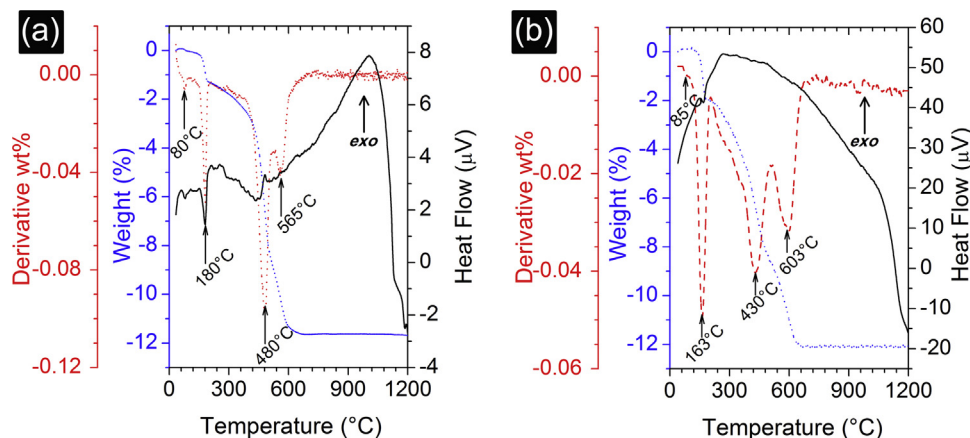


Fig. 2. Thermogravimetric characterization of the KNL–NTS raw mixture obtained by different processing routes: Route I conventional procedure (a), route II by using B-site precursor (b).

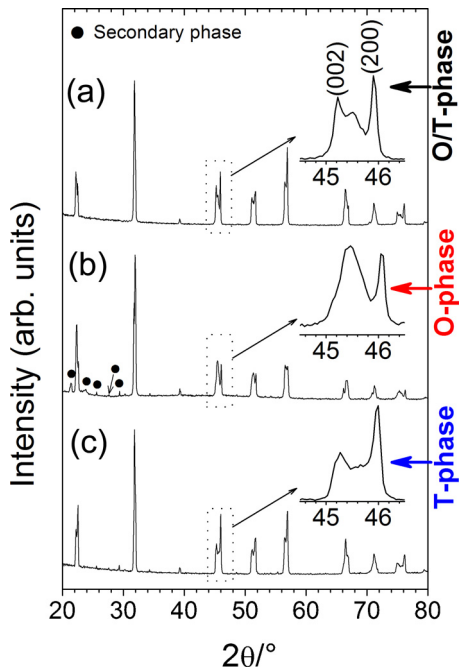


Fig. 4. XRD patterns corresponding to KNL–NTS sintered ceramics: (a) conventional processed samples, Route I, (b) B-site precursor route without sintering bed from the same composition (Route II), and (c) B-site precursor route with the sintering bed of the same composition (Route II-b). The inserts of the Figs. (a–c) show the magnified XRD diffraction pattern in the  $2\theta$  range  $44\text{--}47^\circ$  of the different systems. In addition, a secondary phase was also signalled with a circle symbol (●).

### 3.2. Ceramic systems: structural evolution by XRD and confocal Raman microscopy

The X-ray diffraction patterns of sintered ceramics are shown in Fig. 4(a–c). It can be observed that samples from route II show a perovskite phase and traces of secondary crystalline phases at room temperature which are assigned to  $\text{K}_6\text{LiNb}_6\text{O}_{17}$  or  $\text{K}_6\text{Nb}_{10.88}\text{O}_{30}$ , both with the TTB type structure, Fig. 4(b). The use of the powder bed (protective atmosphere) diminishes the content of secondary phases when the ceramics are sintered (see Fig. 4b and c, respectively). Thus, the B-site route does not prevent the volatilization of the alkali metal elements. Actually, at  $1125^\circ\text{C}$ , the formation of the perovskite as the main phase in all cases is clearly observed. Then, the formation of the KNL–NTS perovskite requires a large diffusion of the different cations involved in the solid solution and is more favoured by the high surface reactivity of the nano-powders obtained by solid state reaction by the decomposition of  $\text{A}_2\text{CO}_3$  to  $\text{A}_2\text{O}$ , as previously observed by Rubio-Marcos et al.<sup>12</sup> For the B-site precursor route, the appearance of the TTB secondary phase could be attributed to different reactivity of the precursor that prolongs exposure of the alkali elements at high temperatures during the sintering step, which promotes their volatilization. Furthermore, it has been reported that volatilization of alkali elements results in the generation of secondary phases and the occurrence of compositional inhomogeneities on KNN-based systems. Consequently, for Li/Ta-modified KNN materials, the TTB secondary phase occurrence was attributed to the

volatilization and segregation of the alkali elements during sintering,<sup>17</sup> which induces an excess of B-site ions through the formation of the TTB phase.

The inserts of the Fig. 4(a–c) display the splitting of the (200) pseudo-cubic peak into (200) and (002), which suggests non-cubic symmetry in these samples. As represented in the insert of the Fig. 4(a–c), the splitting of the (200) pseudo-cubic peak is affected by the processing route. In route I, the ceramic samples present the splitting of the peak indicating the coexistence between tetragonal and orthorhombic symmetry (see insert of the Fig. 4a). However, in the ceramic samples from route II, the (002) peak broadens in samples sintered without powder bed, which probably implies orthorhombic symmetry (insert of the Fig. 4b). Ceramics obtained using a sintering powder bed exhibited higher tetragonal symmetry (insert of the Fig. 4c). The coexistence of different polymorphs (tetragonal and orthorhombic phases), was previously reported in KNL–NTS ceramics for Rubio-Marcos et al.<sup>12</sup> These two different symmetries are difficult to resolve, together with the presence of the TTB phase which presents some common peaks with perovskite structure. As a consequence, the lattice parameters are refined using the tetragonal unit-cell (space group P4mm) for route I and route II with sintering powder bed, and using the orthorhombic unit-cell (space group P222) for route II without sintering powder bed. The calculated parameters revealed an evolution of the lattice parameters,  $a = 3.9545 \pm 0.002 \text{ \AA}$  and  $c = 4.0058 \pm 0.0003 \text{ \AA}$  for KNL–NTS route I (tetragonal symmetry),  $a = 3.9761 \pm 0.002 \text{ \AA}$ ,  $b = 3.9498 \pm 0.0019$  and  $c = 3.9998 \pm 0.0020 \text{ \AA}$  for KNL–NTS route II without sintering powder bed (orthorhombic symmetry) and  $a = 3.9542 \pm 0.0036 \text{ \AA}$  and  $c = 4.0026 \pm 0.0005 \text{ \AA}$  for KNL–NTS route II with sintering powder bed (tetragonal symmetry). In this situation and in order to be able to compare structural distortions for both symmetries, the true tetragonal distortion,  $c/a$ , was used for tetragonal samples, while a pseudo-tetragonality was calculated for orthorhombic samples using a normalized lattice parameter  $a = (a_{\text{ortho}} + b_{\text{ortho}})/2$ . Thus, this evolution is associated with a net decrease of the calculated  $c/a$  ratio from 1.013 (route I) and 1.012 (route II with sintering powder bed) to 1.009 (route II without sintering powder bed). From these diffraction patterns, the appearance of the TTB secondary phase is related to the transformation of the perovskite structure from tetragonal to orthorhombic symmetry.

Fig. 5(a) shows an optical micrograph of the polished surface of the **KNL–NTS route I** ceramic aligned perpendicular to the Raman laser. The  $30 \mu\text{m} \times 30 \mu\text{m}$  area denotes the selected area where the Raman spectra are collected at a plane located just below the surface of the sample where the Raman intensity was maximized. The acquisition time for a single Raman spectrum was 300 milliseconds, thus the acquisition of a Raman image consisting of  $60 \times 60$  pixels (3600 spectra) required 18 min. Features such as Raman peak intensity, peak width and Raman shift from the recorded Raman spectra are fitted with algorithms to compare information and to represent the derived Raman image, Fig. 5(b). From this figure, the main vibrations associated to the  $\text{BO}_6^-$  perovskite octahedron are observed, Fig. 5(c). Thus, the Raman image of the KNL–NTS-Route I ceramic exhibits a high homogeneity of the system. In agreement with XRD patterns,

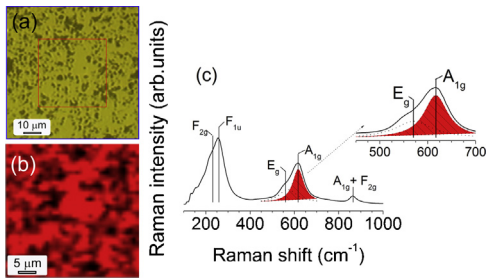


Fig. 5. (a) Optical micrograph of the polished surface of the KNL–NTS ceramic obtained by route I. (b) The Raman image resulted from mapping the different single Raman spectra collected in each pixel. Raman spectra having same spectral shift for the Raman modes were colour identified. The intensity of the colour correlated with the Raman intensity of the KNL–NTS perovskite phase. (c) Average Raman spectra where the insert shows magnified Raman spectra and Lorentzian fits in the frequency range between 450 and 700  $\text{cm}^{-1}$ . These spectra are fitted to the sum of two Lorentzian peaks, ascribed to the E<sub>g</sub> ( $\nu_2$ ) and A<sub>1g</sub> ( $\nu_1$ ) Raman modes, respectively. (For interpretation of the references to color in text, the reader is referred to the web version of the article.)

in Fig. 5(b), secondary phases are not observed and only feature vibrations associated with perovskite phase (marked in red colour on the Fig. 5b) are observed. The vibrations of the BO<sub>6</sub><sup>-</sup> octahedron consist of 1A<sub>1g</sub> ( $\nu_1$ ) + 1E<sub>g</sub> ( $\nu_2$ ) + 2F<sub>1u</sub> ( $\nu_3, \nu_4$ ) + F<sub>2g</sub> ( $\nu_5$ ) + F<sub>2u</sub> ( $\nu_6$ ) modes. From these vibrations, 1A<sub>1g</sub> ( $\nu_1$ ) + 1E<sub>g</sub> ( $\nu_2$ ) + 1F<sub>1u</sub> ( $\nu_3$ ) are stretching modes and the other ones bending modes. A<sub>1g</sub> ( $\nu_1$ ) and F<sub>2g</sub> ( $\nu_5$ ) have been detected as yielding relatively strong scattering in systems similar to the one studied in this paper due to a near-perfect equilateral octahedral symmetry (Raman modes shown in the insert of the Fig. 5c). Changes in the Raman shift of modes associated to the BO<sub>6</sub><sup>-</sup> octahedron allow determining variations in polarization, which are associated with modifications of the constant force of the octahedron due to deformation or stress.<sup>18</sup>

The optical micrographs (Fig. 6a.1 and b.1), Raman images (Fig. 6a.2 and b.2), and the average spectra Raman (Fig. 6a.3 and b.3) of KNL–NTS ceramics using the B-site precursor route are shown in Fig. 6. In the average Raman spectra, the main vibrations associated with BO<sub>6</sub><sup>-</sup> octahedrons of the KNL–NTS perovskite phase can be observed, while in the Raman images the presence of a secondary phase, which is not observed in the average spectra of the ceramics obtained by the route I (see Fig. 5c), can be observed in blue. Fig. 6(a.2) and (b.2) show the localization of the secondary phase which is signalled as blue regions. The average Raman spectrum of the secondary phase is shown in Fig. 6(a.3) and (b.3), which can be indexed on the basis of a phase mixture constituted by a main KNL–NTS phase and a minor secondary phase. A careful examination of the Raman spectra, see Fig. 6(a.3) and (b.3) reveals the presence of Raman modes corresponding to KNL–NTS phase and the appearance of a new Raman peak, as shown in the inserts of the Fig. 6(a.3) and (b.3). The Raman peak, signalled in blue, is attributed to the appearance of a characteristic Raman mode of the TTB phase at  $\sim 686 \text{ cm}^{-1}$ , which emerges concomitantly. A detail of this region is presented in the insets of Fig. 6(a.3) and (b.3), where the spectrum is fitted to the sum of three Lorentzian functions centred at  $\sim 580 \text{ cm}^{-1}$ ,  $\sim 615 \text{ cm}^{-1}$ , and  $\sim 686 \text{ cm}^{-1}$ , and ascribed to the E<sub>g</sub> ( $\nu_2$ ) and A<sub>1g</sub> ( $\nu_1$ ) Raman modes of the KNL–NTS

phase and TTB phase, respectively. This secondary phase corresponds to the TTB phase and its concentration is higher in route II ceramics sintered without using a powder bed. Finally, from the inserts of the Fig. 6(a.3) and (b.3), the secondary phase content for route II ceramics without or with using sintering bed can be calculated, which represent ca. 4.1% and 2.6% of the total measured phases, respectively. Thus, the identification and quantification of secondary phases can be approached by Confocal Raman Microscopy (CRM). It is worth pointing out other characteristics revealed by the CRM imaging since it has been possible to locate the secondary phase (marked as blue regions in Fig. 6a.2 and b.2) previously observed by XRD. According to these results, the secondary phase formation is attributed to the different reagent reactivity which promotes the alkali elements volatilization. Then, the use of a powder bed controls the sintering atmosphere reducing the alkali elements volatilization, the TTB amounts.

### 3.3. Ceramic systems: microstructural characterization

Fig. 7 shows the microstructure of KNL–NTS ceramics sintered at 1125 °C during 2 h, along with the respective grain size distribution diagrams. The followed processing route has a clear effect on microstructure development, especially grain size and morphology of ceramics. The FE-SEM micrographs show the KNL–NTS morphology consisting of faceted grains and cube-shaped grains. The KNL–NTS-Route I ceramics show a porous microstructure containing small grains  $\sim 1.1 \pm 0.6 \mu\text{m}$  without secondary phases (Fig. 7a). KNL–NTS-Route II ceramics sintered without sintering powder bed (Fig. 7b) show larger grain size  $\sim 1.5 \pm 0.8 \mu\text{m}$  and larger elongated grains that resemble secondary phase morphology in spite of their different morphology. KNL–NTS-Route II ceramics sintered with sintering powder bed (Fig. 7c) show an average grain size of  $\sim 1.3 \pm 0.7 \mu\text{m}$  having a reduced presence of cube-shaped grains. In general, the higher B-site homogeneity favours porosity removal and grain growth, while the alkali volatilization produces the appearance of secondary phases. It was stated that in KNN-based ceramics, the formation of a limited amount of liquid phase during sintering promoted the sintering by increasing the solution-precipitation mechanism,<sup>19–21</sup> that resulted in cube-shaped grains. The formation of a liquid phase during sintering of  $(1-x)\text{KNN}-x\text{LiNbO}_3$  is attributed to excess of Na<sub>2</sub>O.<sup>17</sup>

EDS analysis was carried out on the ceramics (Fig. 8) to identify the grain and the secondary phase (i.e. TTB) compositions. The matrix grains (points 1, 2 and 4 of the Fig. 8a, b and c, respectively) have a typical nominal composition with a Na/K ratio  $\sim 1.12$ , 0.90 and 1.02, for the samples corresponding to route I, route II without and with sintering powder bed, respectively. These values are slightly lower than the nominal ratio of 1.18 (see the EDS spectra). The energy dispersion spectrum analysis (EDS) also reveals that the atomic percentages of elements change within the different grains. The concentration and the distribution of Li cannot be detected by the EDS analysis; therefore, its influence on the distribution of the A- and B-site cations cannot be directly assessed. The composition analyses of

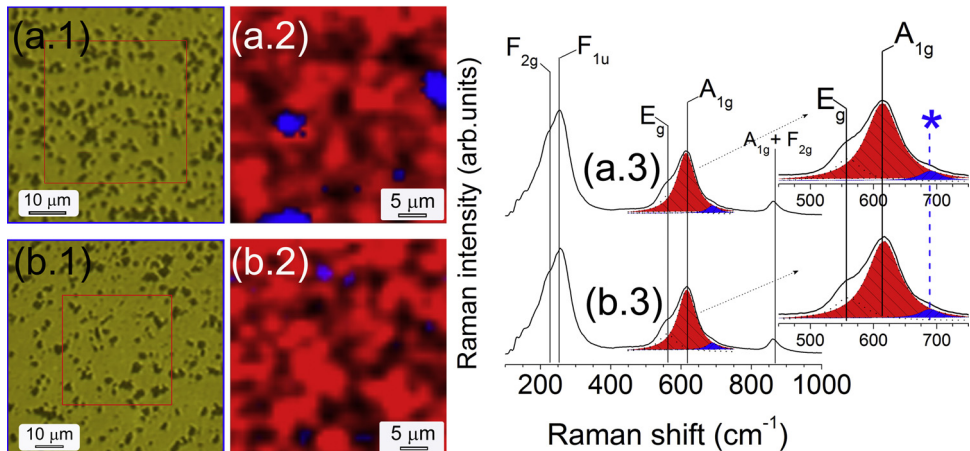


Fig. 6. Detection of the secondary phase observed in the KNL–NTS ceramics obtained by the route II without and with sintering powder bed through confocal Raman spectroscopy: (a.1) and (b.1) Optical micrographs of the polished surface ceramic without and with sintering powder bed. (a.2) and (b.2) Raman image of ceramics without and with sintering powder being, respectively, exhibiting the location secondary phase, blue areas. The Raman image is derived by summing the total spectral pixel intensity from  $150\text{ cm}^{-1}$  to  $1000\text{ cm}^{-1}$ . The secondary phase is signalled in regions with blue colours (\*), whereas the KNL–NTS perovskite phase corresponds to red regions. (a.3) and (b.3) Average Raman spectra of ceramics from route II without and with a sintering powder bed. The inserts of the Figs. (a.3) and (b.3) show magnified Raman spectra and Lorentzian fits in the frequency range between  $450$  and  $750\text{ cm}^{-1}$ . These spectra are fitted to the sum of three Lorentzian peaks, ascribed to the  $E_g(v_2)$ ,  $A_{1g}(v_1)$  corresponding to Raman modes of the KNL–NTS perovskite phase and the third peak is associated with the occurrence of the secondary phase. (For interpretation of the references to color in this figure legend, the reader is referred to the web version of the article.)

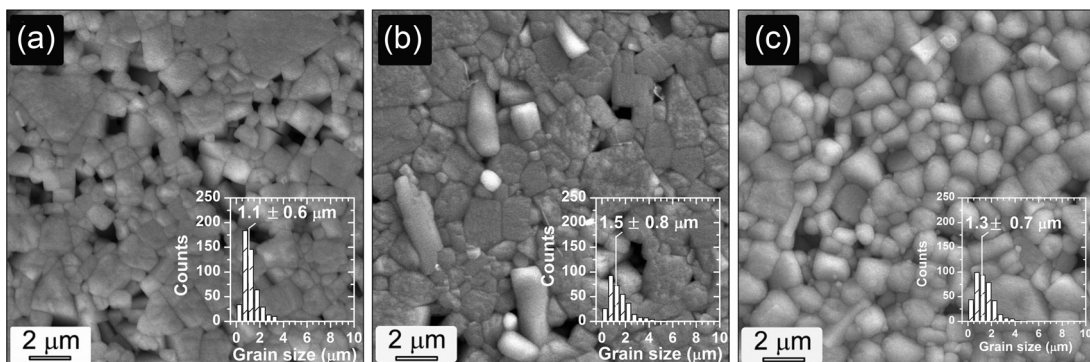


Fig. 7. Microstructure characterization of polished and thermally etched surfaces of KNL–NTS sintered samples: SEM images of (a) route I; (b) route II without sintering powder bed and (c) route II with a sintering powder bed. The insets show the grain size distributions.

all systems are summarized in the Table 1. Na, K, Nb, Sb, and Ta cations were found in the matrix and its composition is confirmed to be very close to the nominal one. The secondary phase shows lower concentration of Na and Ta cations. According to EDS analysis, the secondary phase (point 3 and 5, Fig. 8b–c) is quite similar to that of  $\text{Li}_x(\text{K}_{0.78}\text{Na}_{0.22})_6(\text{Nb}_{0.86}\text{Ta}_{0.10}\text{Sb}_{0.04})_{10.9}\text{O}_{30}$  tungsten bronze material,<sup>22</sup> although our results reveal that the TTB phase grains present slight variations in Na-composition. Therefore, considering the aforementioned observations in the structural characterization section (XRD and CRM), the

appearance of secondary phase is related to the alkali volatilization. Moreover, the use of sintering powder bed prevents the alkali volatilization and it modifies the final microstructure.

#### 3.4. Ceramic systems: electrical properties

Table 2 shows density, average grain size, real part ( $\epsilon_{33}$ ) of dielectric permittivity, dielectric loss ( $\tan \delta$ ) and piezoelectric constant of sintered samples. It can be observed that KNL–NTS-Route I ceramics show slightly lower density

Table 1  
Composition calculated from the different EDS spectra in atomic percentage (% atom).

KNL–NTS	O	Na	K	Nb	Sb	Ta	Na/K	
Route I	(1)	60.76	9.67	8.59	17.93	0.84	2.21	1.12
Route II without bed	(2)	62.90	7.12	7.89	18.29	0.92	3.46	0.90
	(3)	64.41	2.71	9.57	20.76	0.48	2.07	0.28
Route II with bed	(4)	61.86	8.46	8.28	18.32	0.40	2.68	1.02
	(5)	61.87	6.40	10.33	18.54	0.33	2.54	0.62

Table 2

Density ( $\rho$ ), average grain size ( $D_{50}$ ), dielectric properties ( $\varepsilon_{33}$ ,  $\tan(\delta)$ ), piezoelectric constant ( $d_{33}$ ) and remnant polarization values ( $P_r$ ) of sintered samples.

KNL-NTS	$\rho$ (g/cm <sup>3</sup> )	$D_{50}$ (μm)	$\varepsilon_{33}$	$\tan(\delta)$	$d_{33}$ (pC/m)	$P_r$ (μC/m <sup>2</sup> )
Route I	$4.41 \pm 0.02$	$1.1 \pm 0.5$	880	0.010	230	22.9
Route II	$4.43 \pm 0.01$	$1.5 \pm 0.8$	635	0.011	140	18.8
Route II with bed	$4.54 \pm 0.03$	$1.3 \pm 0.7$	685	0.005	170	17.6

values than samples using the B-site precursor, as well as higher  $\varepsilon_{33}$ ,  $d_{33}$  and  $P_r$  values. This behaviour seems to correlate higher grain size with poor dielectric and piezoelectric properties. In this way, grain size increase could also correlate with formation of secondary phases due the alkaline volatilization. However a depth analysis is required.

Real permittivity and dielectric losses as a function of frequency and processing route are shown in Fig. 9(a) and (b), respectively. Ceramics from the B-site precursor route present the lowest real permittivity values in the studied frequency range. This effect could be associated to higher homogeneity of B-site cations in addition to larger grain size. At low frequencies the real permittivity shows a marked decrease and high dielectric losses,

which could be related to a space charge relaxation process. Moreover, the influence of frequency on dielectric properties, at the lowest frequency range, is less pronounced in ceramics from the B-site precursor route.

The real permittivity and loss tangent variation versus temperature at 50 kHz are represented in Fig. 10. It is well known that KNL-NTS ceramics present three polymorphic phase transitions (PPT) on heating; rhombohedral to orthorhombic (r-o) transition, orthorhombic to tetragonal (o-t) transition at room temperature and tetragonal to cubic (t-c or Tc) transitions.<sup>23</sup> According to Fig. 10 two peaks in the range of 25–600 °C can be observed for route I ceramics. The lower temperature peak occurs at RT and is related to  $T_{o-t}$ . The higher one corresponds to the Curie temperature ( $T_c$ ) at 280 °C. In route II ceramics,  $T_c$  and  $T_{o-t}$  increase having  $T_{o-t}$  and  $T_c$  values around 63 °C and 335 °C, and 77 °C and 330 °C for route II ceramics without and with sintering powder bed, respectively. Thus, in ceramics processed through route II, orthorhombic-tetragonal phase transition temperature moves to higher temperatures.

Based on phenomena observed in KNL-NTS route I ceramics, which show high tetragonal symmetry, absence of secondary phases and lower Curie temperature ( $T_c$ ), we can suggest that the difference in  $T_c$  could be attributed to different effects. First, a phase transition  $T_{o-t}$  increase when Li is retained in TTB phase has been reported.<sup>24</sup> The small radius of  $\text{Li}^+$  produces the

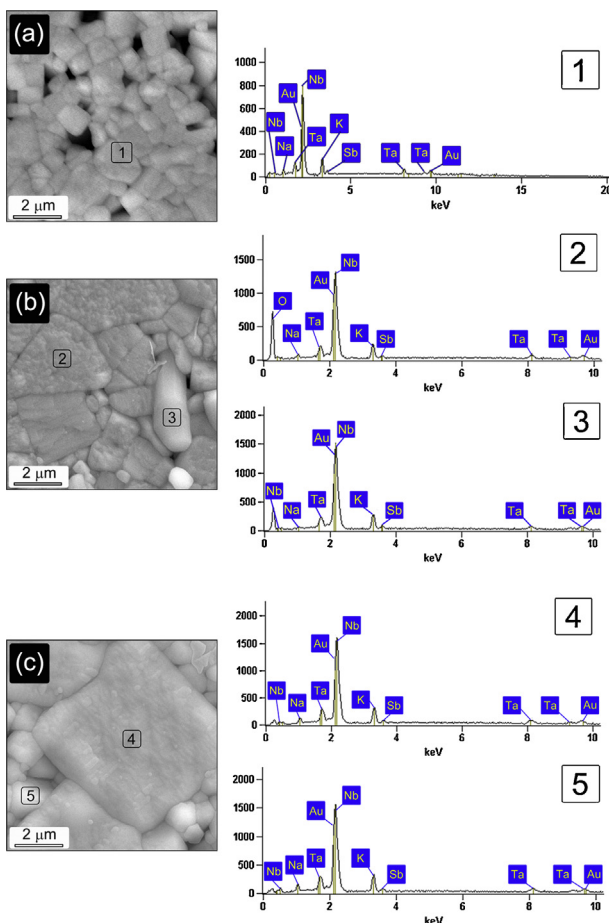


Fig. 8. Evaluating the secondary phase composition in the different systems of the KNL-NTS sintered ceramics: Micrographs and Energy Dispersive Spectra (EDS) of: (a) route I, (b) route II without sintering powder bed and (c) route II with a sintering powder bed. EDS spectra collected at the different regions: (i) Grains with nominal compositions (1, 2 and 4) and (ii) grains of the secondary phase (3 and 5).

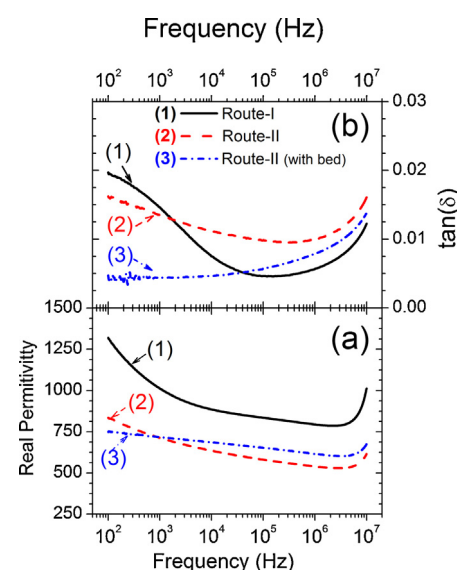


Fig. 9. (a) Real permittivity and (b) loss tangent vs frequency for KNL-NTS ceramics measured at room. The ceramic routes represented in Fig. (a-b) are the following: (1) route I; (2) route II without sintering powder bed; (3) route II with a sintering powder bed.

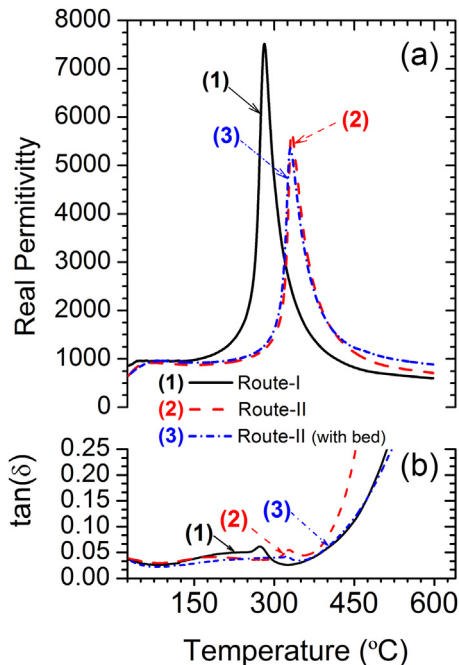


Fig. 10. (a) Real permittivity ( $\epsilon'$ ) and (b) loss tangent as a function of temperature of KNL–NTS (at 50 kHz). The ceramic routes represented in Fig. are the following: (1) route I; (2) route II without sintering powder bed and (3) route II with a sintering powder bed.

crystalline lattice distortion and increases the tetragonal ratio, so when lithium content is reduced, the crystalline lattice distortion is not so extended. Therefore, ceramics processed through the B-site precursor route show high  $T_{0-t}$  temperature, due to tantalum and lithium retention in the TTB. Second, the cationic disorder in A or B-sites is evidenced through the expansion of the transitions, consequently, this phenomenon could be discarded. Third, the differences in grain size do not affect greatly the transition temperatures due to their similarities. Fourth, EDS shows different concentrations of Ta on KNL–NTS phases ceramics processed through route II depending on the sintering atmosphere variation when the sintering powder bed is used.

Finally, ferroelectric hysteresis loops of KNL–NTS at room temperature are shown in Fig. 11. KNL–NTS-route I ceramics reach higher values of the main ferroelectric parameter as saturation polarization,  $P_s = 26 \mu\text{C}/\text{cm}^2$  remnant polarization  $P_r = 22.9 \mu\text{C}/\text{cm}^2$  and coercive field  $E_c = 21 \text{kV}/\text{cm}$ , than route II ceramics. The hysteresis loop of the ceramics processed through route I is more conductive in accordance with the highest dielectric losses corresponding to the space charge polarization process. Moreover, the higher the tetragonality ratio of ceramics processed through the route I, the higher the tetragonality degree.

Ceramics processed through route II show a decrease in all ferroelectric parameters. The decrease in the dielectric losses results in a more saturated and less conductive hysteresis loop. However, the low tetragonality ratio reduces the remnant polarization, as well as the  $d_{33}$  coefficient. The  $T_{0-t}$  transition shifts towards higher temperatures stabilizing low temperature domains (orthorhombic or monoclinic

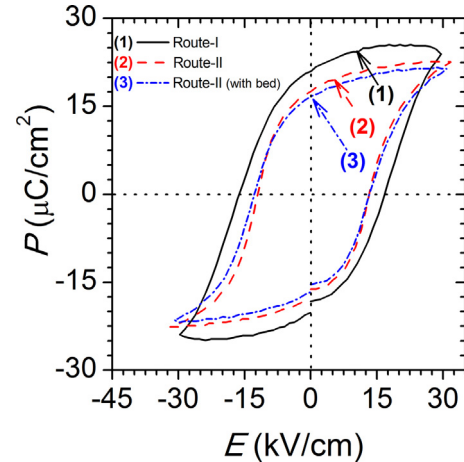


Fig. 11. Ferroelectric hysteresis loops at room temperature for KNL–NTS ceramics. The ceramic routes represented in Fig. are the following: (1) route I; (2) route II without sintering powder bed; (3) route II with a sintering powder bed.

domains). The phase coexistence including low temperature domains restricts the domain wall movement and therefore the polarization is decreased. In ceramics processed through route II and sintered with a powder bed, the dielectric losses reduction improves the effective electric field and a higher polarization level is reached. Moreover, the conductive mechanism in KNN-based ceramic requires more attention because its influence on piezoelectric properties is not well established.

#### 4. Conclusions

The effect of B-site precursor route on final microstructure, phase transition and electric properties of KNL–NTS systems obtained by the conventional mixed oxide method has been reported. X-ray diffraction patterns show the formation of a perovskite-phase corresponding to KNL–NTS solid solution. In this case, two different symmetries are presented (tetragonal and orthorhombic), together with the formation of a secondary phase with a TTB structure in samples prepared following the B-site precursor route. The improved piezoelectric and dielectric properties of samples obtained through the conventional route is correlated with higher density, the absence of secondary phases and lower temperatures for orthorhombic to tetragonal phase transition. Ceramics processed by using B-site precursor show different crystalline structures as a function of sintering conditions or K/Na ratio. Larger differences are observed in ceramics sintered with a sintering powder bed due to a reduction in alkaline volatilization that prevents formation of liquid TTB phase. Furthermore, samples sintered using a powder bed result in an improvement of the final properties. The reduction of the low frequency dielectric losses improved the piezoelectric coefficients. Further studies of the conduction mechanism in KNN-based piezoceramics are envisaged to progress in the understanding of polarization mechanisms and thereafter the piezoelectric properties.

## Acknowledgment

The authors are grateful to CONICET, ANCPyT (Argentina) and MICINN project MAT 2010-21088-C03-01 for the financial support provided for this research. Dr. F. Rubio-Marcos is also indebted to CSIC for a “Junta de Ampliación de Estudios” contract (ref. JAEDOC071).

## References

- Saito Y, Takao H, Tani T, Nonoyama T, Takatori K, Homma T, et al. Lead-free piezoceramics. *Nature* 2004;432:84–7.
- Wang H, Zuo R, Liu Y, Fu J. Densification behavior, microstructure, and electrical properties of sol–gel-derived niobium-doped  $(\text{Bi}_{0.5}\text{Na}_{0.5})_{0.94}\text{Ba}_{0.06}\text{TiO}_3$  ceramics. *J Mater Sci* 2010;45:3677–82.
- Ramajo L, Parra R, Ramírez MA, Castro MS. Electrical and microstructural properties of  $\text{CaTiO}_3$ -doped  $\text{K}_{1/2}\text{Na}_{1/2}\text{NbO}_3$ -lead free ceramics. *Bull Mater Sci* 2011;34:1213–7.
- Biroi H, Damjanovic D, Setter N. Preparation and characterization of  $(\text{K}_{0.5}\text{Na}_{0.5})\text{NbO}_3$  ceramics. *J Eur Ceram Soc* 2006;26:861–6.
- Rubio-Marcos F, Romero JJ, Martín-Gonzalez MS, Fernández JF. Effect of stoichiometry and milling processes in the synthesis and the piezoelectric properties of KNN-modified nanoparticles by solid state reaction. *J Eur Ceram Soc* 2010;30:2763–71.
- Zhen Y, Li JF. Normal sintering of  $(\text{K},\text{Na})\text{NbO}_3$ -based ceramics: influence of sintering temperature on densification, microstructure, and electrical properties. *J Am Ceram Soc* 2006;89:3669–75.
- Hollenstein E, Davis M, Damjanovic D, Setter N. Piezoelectric properties of Li- and Ta-modified  $(\text{K}_{0.5}\text{Na}_{0.5})\text{NbO}_3$  ceramics. *Appl Phys Lett* 2005;87:182905.
- Venkatesh JV, Sherman V, Setter N. *J Am Ceram Soc* 2005;88:3397–404.
- Hill VG, Chang LLY, Harker RI. Subsolidus stability relations in the system  $\text{KTaO}_3$ – $\text{KNbO}_2$ . *J Am Ceram Soc* 1968;51:723–4.
- Jenko D, Bencan A, Malic B, Holc J, Kosec M. Electron microscopy studies of potassium sodium niobate ceramics. *Microsc Microanal* 2005;11:572–80.
- Wang Y, Damjanovic D, Klein N, Hollenstein E, Setter N. Compositional inhomogeneity in Li- and Ta-modified  $(\text{K}, \text{Na})\text{NbO}_3$  ceramics. *J Am Ceram Soc* 2007;90:3485–9.
- Rubio-Marcos F, Romero JJ, Fernandez JF. Effect of the temperature on the synthesis of KNN-modified nanoparticles by a solid state reaction route. *J Nanopart Res* 2010;12:2495–502.
- Rubio-Marcos F, Romero JJ, Ochoa DA, García JE, Perez R, Fernández JF. Effects of poling process on KNN-modified piezoceramic properties. *J Am Ceram Soc* 2010;93:318–21.
- Rojac T, Kosec M, Šegedin P, Malič B, Holc J. The formation of a carbonato complex during the mechanochemical treatment of a  $\text{Na}_2\text{CO}_3\text{Nb}_2\text{O}_5$  mixture. *Solid State Ionics* 2006;177:2987–95.
- Heda PK, Dollimore D, Alexander KS, Chen D, Law E, Bicknell P. A method of assessing solid state reactivity illustrated by thermal decomposition experiments on sodium bicarbonate. *Thermochim Acta* 1995;255:255–72.
- Harris MJ, Salje EKH. The incommensurate phase of sodium carbonate: an infrared absorption study. *J Phys Condens Matter* 1992;4:4399–408.
- Wang Y, Damjanovic D, Klein N, Setter N. High-temperature instability of Li- and Ta-modified  $(\text{K},\text{Na})\text{NbO}_3$  piezoceramics. *J Am Ceram Soc* 2008;91:1962–70.
- Rubio-Marcos F, Marchet P, Romero JJ, Fernández JF. Structural, microstructural and electrical properties evolution of  $(\text{K},\text{Na},\text{Li})(\text{Nb},\text{Ta},\text{Sb})\text{O}_3$  lead-free piezoceramics through NiO doping. *J Eur Ceram Soc* 2011;31:2309–17.
- Rubio-Marcos F, Ochoa P, Fernández JF. Sintering and properties of lead-free  $(\text{K},\text{Na},\text{Li})(\text{Nb},\text{Ta},\text{Sb})\text{O}_3$  piezoceramics. *J Eur Ceram Soc* 2007;27:4125–9.
- Rubio-Marcos F, Marchet P, Merle-Méjean T, Fernández JF. Role of sintering time, crystalline phases and symmetry in the piezoelectric properties of lead-free KNN-modified ceramics. *Mater Chem Phys* 2010;123:91–7.
- Kim SJ, Kang CY, Choi JW, Kim HJ, Sung MY, Yoon SJ. Low temperature sintering of  $\text{ZnO}$ -doped  $0.01\text{Pb}(\text{Mg}_{1/2}\text{W}_{1/2})\text{O}_3\text{–}0.41\text{Pb}(\text{Ni}_{1/3}\text{Nb}_{2/3})\text{O}_3\text{–}0.35\text{PbTiO}_3\text{–}0.23\text{PbZrO}_3$ , ceramics. *Jpn J Appl Phys* 2007;46:276–9.
- Tanaka J, Onoda Y, Tsukioka M, Shimazu M, Ehara S. The NMR study of Li ion motion in  $\text{K}_3\text{LiNb}_6\text{O}_{17}$  and  $\text{K}_3\text{LiTa}_6\text{O}_{17}$ . *Jpn J Appl Phys* 1981;21:451–5.
- Vendrell X, García JE, Rubio-Marcos F, Ochoa DA, Mestres L, Fernández JF. Exploring different sintering atmospheres to reduce nonlinear response of modified KNN piezoceramics. *J Eur Ceram Soc* 2013;33:825–31.
- Xu SL, Lee JH, Kim JJ, Young LH, Cho SH. Effect of  $\text{Nb}_2\text{O}_5$  content on dielectric characteristics of tungsten-bronze-structured KLN ceramics. *Mater Sci Eng B* 2003;99:483–6.